
Multi-Type Point Cloud Autoencoder: A Complete Equivariant Embedding for Molecule Conformation and Pose

Michael Kilgour

Department of Chemistry, New York University
michael.kilgour@nyu.edu

Mark E. Tuckerman

Courant Institute of Mathematical Sciences, New York University
NYU-ECNU Center for Computational Chemistry at NYU Shanghai
Simons Center for Computational Physical Chemistry at New York University
mark.tuckerman@nyu.edu

Jutta Rogal

Department of Chemistry, New York University
Fachbereich Physik, Freie Universität Berlin
jutta.rogal@nyu.edu

Abstract

The point cloud is a flexible representation for a wide variety of data types, and is a particularly natural fit for the 3D conformations of molecules. Extant molecule embedding/representation schemes typically focus on internal degrees of freedom, ignoring the global 3D orientation. For tasks that depend on knowledge of both molecular conformation and 3D orientation, such as the generation of molecular dimers, clusters, or condensed phases, we require a representation which is provably complete in the types and positions of atomic nuclei and roto-inversion equivariant with respect to the input point cloud. We develop, train, and evaluate a new type of autoencoder, molecular $O(3)$ encoding net (Mo3ENet), for multi-type point clouds, for which we propose a new reconstruction loss, capitalizing on a Gaussian mixture representation of the input and output point clouds. Mo3ENet is end-to-end equivariant, meaning the learned representation can be manipulated on $O(3)$, a practical bonus for downstream learning tasks. An appropriately trained Mo3ENet latent space comprises a universal embedding for scalar and vector molecule property prediction tasks, as well as other downstream tasks incorporating the 3D molecular pose.

1 Introduction

Point clouds are an extremely flexible data type used in many 3D modelling applications [1]. While often used as a primitive representation for the surface of some object [2], point clouds are also a natural representation for molecular information [3, 4, 5]. Indeed, in the most common file formats for 3D atomistic molecular data encode a simple list of points and associated atom types, that is, a multi-type point cloud. Despite extensive prior work in both point cloud modelling and molecular representations, no extant model explicitly decomposes 3D molecular structures to a fixed-size

equivariant latent embedding, and then reconstructs them in atomistic detail without any scaffolding, sampling, or other external information.

Such an autoencoder would be a useful tool in several problem areas. The perhaps most exciting application is in the growing field of machine learning for molecular materials design [6, 7, 8, 9, 10, 11, 12, 13, 14, 15], where one may need to condition a downstream task on the precise geometry *and* rotational orientation of an input molecule, in the form of an embedding vector prepared by the encoder.

Further, such an encoder represents the ‘ultimate’ brute-force answer to the molecule representation learning problem. Currently, it is common practice to co-train molecule representation and property prediction models [16, 17] in the form of graph neural networks, although there is also impressive recent work on extensively pretrained representation models [18]. Co-training is generally an efficient approach, allowing one to make good use of finite datasets. However, in the limit of large datasets and a well-converged pretrained autoencoder model, we can obviate the need for complex and sometimes challenging-to-train graph neural networks, and train simple and reliable multilayer perceptrons directly on our encoder embedding.

Finally, the decoder half of this autoencoder would be a new and potentially interesting generative model for molecular data, with property-driven sampling and search enabled by conditional training and careful engineering of the embedding space. In the approach presented here, the decoder has the additional advantage of sampling in a single forward pass of the model, as opposed to modern diffusion approaches which may require a number of forward passes to generate a single sample [19, 20, 21, 22].

With our work, we advance the field of point cloud learning by developing a new reconstruction loss and model architecture for multi-type point clouds which is smooth and fast to compute, returns trainable gradients, and allows for varying input composition and size. We leverage developments in equivariant graph learning for point-structured data [23, 4, 24], to develop and optimize an end-to-end equivariant autoencoder model. If accurately converged, the latent $O(3)$ equivariant embedding between encoder and decoder in this model must necessarily contain the complete 3D coordinate and type information about a given molecule, and therefore serve as a universal embedding space for molecular data. Such an embedding could be leveraged for any downstream task dependent on molecular structure *and/or* pose, without fear of common issues in graph learning such as lack of representational power [3], with the added benefit of rotatability.

Our Mo3ENet model comprises an equivariant graph neural network (EGNN) encoder, which embeds an input point cloud as a fixed dimensional equivariant representation $\vec{g}_{k \times 3}$, and an equivariant multilayer perceptron (EMLP) decoder. The encoder is flexible in the number of input points, and the output returns a fixed-size ‘swarm’ of output points. Using a ‘swarm’ decoder with a fixed number of output points enables us to use a simple and efficient MLP-type model as the decoder, rather than a more complex graph or sequence model. A large swarm size with learnable weights ensures flexibility of the decoding with respect to input size and composition. Both inputs and outputs are mapped to Gaussian mixtures (GMs), and their pairwise overlaps computed to determine the reconstruction fidelity. Training is facilitated by an reduction of the GMs’ widths until neighboring points no longer significantly overlap, and the distance between input and output distributions is minimized, corresponding to perfect reconstruction of the input point cloud.

As an illustration of our autoencoder model in a chemistry context, we use a large and diverse set of molecules as a source of training data and assess its representation ability on this dataset on equivariant reconstruction and property prediction tasks.

2 Related work

Point cloud generation

Given their utility, there is vast prior literature on point cloud learning, including object classification, semantic segmentation, generative modelling, representation learning, and much more [25, 26, 2, 27, 28, 29]. Various model architectures have been proposed to process this data type, with inputs cast as voxel grids, meshes, and real-space graphs. Models incorporating underlying physical equivariances into their building blocks have also seen increased uptake in recent years [30, 24, 31, 32], with particular popularity in the chemical modelling community [33, 23, 4]. In this vein, several generative

approaches including various autoencoders [2, 34] and generative adversarial networks [35, 36], have been developed, with particular focus on point cloud reconstruction. While many insights from this field, and particularly the original PointNet architecture [37], have been influential in molecular modelling, there are as yet limited tools for the analysis and generation of point clouds with multiple types.

Molecule representation learning

The study of molecule representations goes back decades in the chemistry literature. Such approaches run the gamut from straightforward and interpretable, such as the bag of bonds [38] or SMILES strings, to the more structurally-informed Coulomb matrix [39], to physics-inspired descriptors [40, 41], and on to high-dimensional learned embeddings [42, 18, 43, 44].

The most powerful pretrained approach currently appears to be the Uni-Mol framework [18], which combines a large and powerful graph model, self-supervised learning, property prediction, and very large datasets, to train a high-quality molecule representation. Despite impressive benchmark performance, however, Uni-Mol does not explicitly encode and decode the complete molecular 3D structure.

Many generative models for molecules have been developed, including a number of autoencoders [33, 45, 46, 47, 48, 49, 50, 51], though these generally either work in the space of nodes and edges (so-called ‘2D’ structure), rather than 3D coordinates, are not generalizable between molecules, or do not encode to a single molecule-wide embedding of fixed size, without any scaffolding provided to assist reconstruction, and none return a complete and equivariant (rotatable) embedding.

3 Models and methods

3.1 Training

We trained on the QM9 dataset [52, 53], containing 133k molecules with up to 9 heavy atoms, including H, C, N, O, and F. We optimized models including and excluding hydrogen atoms, both to compare performance and because in many relevant datasets such as the Cambridge Structural Database [54] of molecular crystals, hydrogen positions are inconsistent or absent. Insights from training on QM9 should be transferable to training on larger datasets with larger molecules, e.g., GEOM [55], QMugs [56]. The dataset was split 80:20 into train:test to assess generalization to unseen molecules.

We also attempted training with point clouds from a random uniform distribution in both coordinates and atom types, but found negligible benefit to model performance on molecular data. This should, perhaps, not be surprising, since molecular information is structured by certain common correlations, such as bond lengths and angles, which the autoencoder can exploit to more easily reconstruct the input. Random point clouds share none of these correlations and, thus, are far outside the distribution of molecular data.

3.2 Model architecture

The autoencoder is comprised of an encoder and decoder, inputting and outputting scalars s and vectors \vec{v} . In the molecular context, the initial nodewise scalar inputs s are the atom types and radial distances from the molecule centroid, and vector inputs \vec{v} are the Cartesian point vectors from the molecule centroid. The model is end-to-end equivariant on $O(3)$, that is, rotations and inversions of the input result in identical rotations to the embedding and decoding. As illustrated in Figure 1(a), during a forward pass, the atoms in a given molecule are embedded as nodes in a graph, nonlinearly transformed, and aggregated to a fixed size latent embedding, \vec{g} , which is decoded to a swarm of points \vec{d} .

The primary building blocks of our model are an equivariant multilayer perceptron (EMLP), graph convolution layers, and graph-wise aggregators. In constructing these modules, we borrow concepts from prior works on equivariant models on scalars and vectors [23, 4, 24], which process directly the point positions in Cartesian space. Only a few transformations of vector features retain $O(3)$ equivariance; we nevertheless realize a flexible model using the following basic operations: (1) linear combination, $\vec{v}^{t+1} = \sum_j c_j \vec{v}_j^t$, (2) adjustment of vector lengths via multiplication by scalars, and (3)

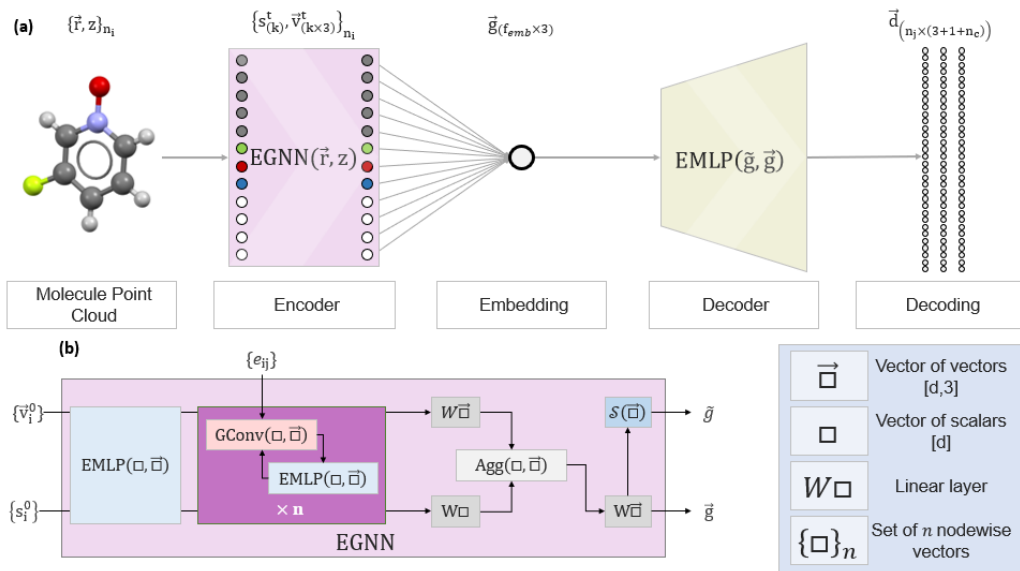


Figure 1: (a) Overall summary of autoencoder architecture. Molecule point cloud coordinates, \vec{r} and atom types z are embedded and bottlenecked to dimension f_{emb} by the encoder. Then, the decoder transforms the embedding to n_j independently weighted points in the $3 + 1 + n_c$ dimensional output cloud, where n_c is the number of classes or types in the dataset and one extra dimension for the learned weights. (b) Outline of the architecture of the equivariant graph model which comprises the encoder, outputting the equivariant embedding \vec{g} and its scalarized counterpart \tilde{g} .

vector embedding and activation, similar to the projection scheme developed in [24], as well as the usual neural network operations for scalars. Full technical details of model construction are provided in the supplemental material (SM).

The encoder model, shown in Figure 1(b) is comprised of an embedding step, alternating EMLP and graph convolution modules, and finally graph aggregation. A ‘scalarizing’ module \mathcal{S} , can also be used to generate a rotation invariant scalar representation of the full vector embedding. The decoder is a straightforward EMLP model, returning scalar and vector features of the output swarm.

$$\begin{aligned} s^N, \vec{v}^N &= \text{EMLP}(\tilde{g}, \vec{g}) \\ \vec{d} &= \vec{v}^N \parallel s^N \end{aligned} \quad (1)$$

\vec{d} is a vector with shape $n_j \times (3 + n_c + 1)$, corresponding to the n_j output swarm nodes, the 3 Cartesian dimensions, the n_c classwise probabilities, and the raw amplitude of the nodewise weight. The decoder is equivariant with respect to the Cartesian dimensions and invariant with respect to type and weight. The n_c elements are normed via softmax within each node to a particle-type probability. Each output point also outputs a learnable weight w_j computed as the softmax over the predicted amplitude for all points in the output swarm, multiplied by the number of atoms in the input graph, such that $\sum_j w_j = n_i$.

3.3 Reconstruction loss

To train a multi-type point cloud autoencoder, we develop a reconstruction loss function with the following properties: smoothly converging in particle positions and type variations, fast to evaluate, permutation invariant, scales easily to large numbers of particles and particle types, and provides a trainable gradient.

We cast input and output point clouds as point-centred Gaussian mixtures in the 3 Cartesian plus n_c point type dimensions (corresponding practically to atom types, H, C, N, O, F,...). For example, a hydrogen atom with Cartesian coordinates x, y, z would have coordinates $(x, y, z, 1, 0, 0, 0, \dots)$, and a carbon atom $(x, y, z, 0, 1, 0, 0, \dots)$.

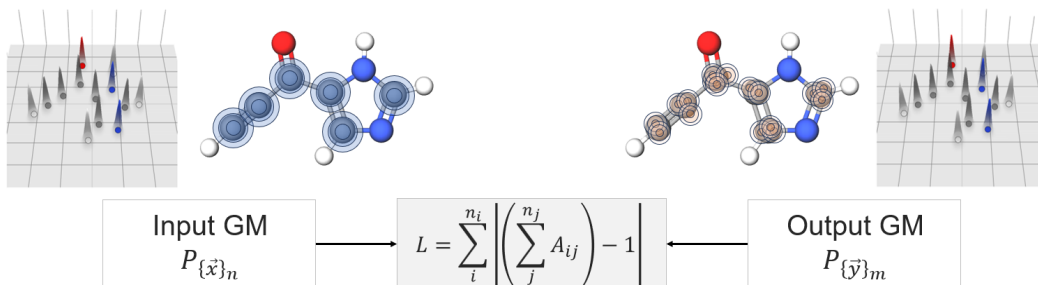


Figure 2: Illustrative diagram demonstrating the correspondence between point clouds and Gaussian Mixtures. We show the explicit GMs projecting in different colors each type dimension as well as cartoons of point-centered Gaussians, projected in the ‘carbon’ dimension. These GMs are compared pairwise over input and output points to determine the overall overlap with each input node.

In the convergent limit, diagrammed in Figure 2, each point in the input should be exactly overlapped by the GM of the output. The input GM is centred on the Cartesian points in the input cloud and one-hot encoded in the n_c type dimensions, with a variable number of points n_i . The output GM is likewise constructed, centred in the points in the output distribution, with learned probabilities for each particle type dimension, a fixed number of points n_j predicted by the decoder, and appropriately normed to a total probability mass matching the input GM. The output comprises a fixed number of points in a ‘swarm’, n_j , with n_j in practice significantly greater than n_i .

The decoder could be designed as a graph model, mirroring the encoder, though we found empirically that this type of model failed to train, and required auxiliary information outside the fixed-size latent embedding (i.e., the number of atoms in the molecule). Instead, considering the decoder as an EMLP simplifies the architecture and demonstrates efficient learning, afforded by the fact that our GM reconstruction loss does not require the number of points in input and output distributions to be equal.

The overlap between points i and j in the input and output, respectively, is simply given by their Gaussian distributed euclidean distances,

$$A_{ij}(\vec{x}_i, \vec{y}_j) = w_j \cdot e^{-\frac{d_{ij}^2}{\sigma}}, \quad (2)$$

with d_{ij} as the euclidean distance between points \vec{x}_i and \vec{y}_j , $\vec{x}_i = \vec{r}_i \| e_i$, \vec{r}_i the 3D coordinate, and $e_i = c_T \cdot \text{OneHot}(z_i)$ a one-hot encoding for the type of particle i . w_j is, again, the learned weight for output node j . The predicted points j are similarly encoded as $\vec{y}_j = \vec{r}_j \| (c_T \cdot P(z_j))$, with the normalized probabilities over particle types substituted for the one-hot encoding. c_T is a scaling factor which adjusts the relative distances between particle types. It is a tunable hyperparameter which can have significant impact on the training dynamics if taken too large or too small compared to σ . In principle, we expect to see good performance when c_T is taken on the order of interatomic distances, typically 2\AA , such that atoms of different types are neither too close, such that they overlap, or too far, such that the type space becomes too sparse.

For $\sigma \ll$ the minimum inter-particle distance, the input and output GMs are matched when the pairwise overlaps of the outputs with each input particle sum to unity. Therefore, the per-particle loss is simply the sum of pairwise overlaps from $j \rightarrow i$

$$L = \sum_i^{n_i} \left| \left(\sum_j^{n_j} A_{ij} \right) - 1 \right|. \quad (3)$$

In practice, we initialize σ somewhat large to ensure the decoder receives nonzero losses and therefore gradients at the beginning of training. In such early stages, the loss is the difference between the input-output overlap and the input self-overlap, from adjacent points’ Gaussians intruding on one-another,

$$L = \sum_i^{n_i} \left| \left(\sum_j^{n_j} A_{ij} \right) - \left(\sum_k^{n_i} A_{ik} \right) \right|. \quad (4)$$

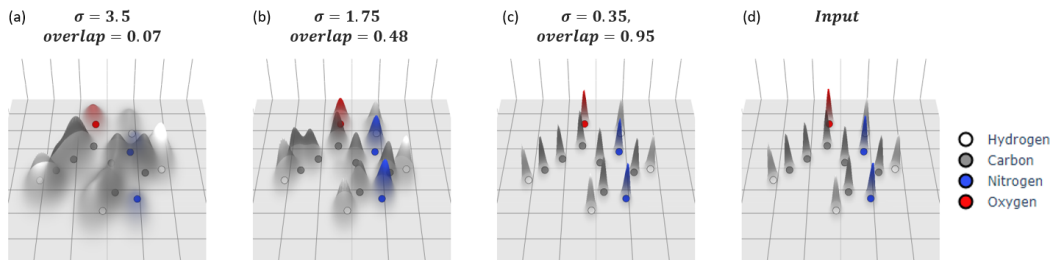


Figure 3: (a), (b), and (c) Convergence of the output Gaussian mixture on a flat molecule (point cloud shown), while reducing the Gaussian width, projecting each of the typewise dimensions in individual colors. (d) Input GM.

A converging series of decoder output GMs for a given molecule is shown in Figure 3. As the reconstruction loss improves, σ is reduced, increasing the problem difficulty, until the overlap between points in the input becomes negligible.

We experimented with several alternate or auxiliary losses, for example, one enforcing the correct distribution of atom types in the decoder output, with the goal of accelerating model convergence. In practice, however, these did not generally improve model performance, possibly due to limiting the optimization pathways for the basic reconstruction loss. Two exceptions were employed to ensure robust gradients in early training.

$$L_c = \sum_j^{n_j} \text{Max}\{(\|\vec{r}_j\| - 1), 0\} \quad (5)$$

constrains output points to be within the unit sphere of the origin, which is the maximum span of all the input point clouds. This prevents decoded points straying too far from the range of the input, which would lead to vanishingly small gradients from the reconstruction loss. Secondly, since we empirically observed some point weights vanishing in early epochs and inhibiting convergence, we implement a constraint on the minimum allowable output point weight w_j , at 1% of the mean for a given output swarm. In practice, both constraining losses converge trivially and do not seem to constrain optimization against the reconstruction loss.

3.4 Distance Calculation

Beyond the reconstruction loss, which is somewhat abstract in chemical structure terms, we calculate the root mean squared distance (RMSD) between input and output point clouds. To accomplish this, the output points are first clustered into predicted particle types and positions, to match against the inputs. When given a molecular scaffold, this can be straightforwardly done by assigning any output cloud points j within less than half a bond length of inputs i to cluster i , and aggregating them by their respective weights. In the case of no molecular scaffold, such as during *de novo* generation or conformational transformation, agglomerative clustering is performed on the output swarm in the Cartesian dimensions, followed by a merge of low-weight clusters into their nearest neighbors.

Both of these approaches qualitatively agree with visual inspection and the reconstruction loss in the range of small deviations, where the output swarm particles from a trained autoencoder model are generally tightly clustered around the predicted particle positions. When the output swarm is diffuse, meaning the reconstruction is under-converged, the reconstruction loss is large, and both clustering approaches fail. In other words, these clustering approaches only return sensible results when applied to an already reasonably good reconstruction.

3.5 Training protocol

During training, when the loss reaches a certain lower threshold, we gradually decrease σ such that eq. (4) converges to eq. (3). This gradually increases the difficulty of the problem, as the target distribution narrows, until the mean self-overlap of the input samples is below 0.0005. All model hyperparameters and further training details are given in the supplemental material.

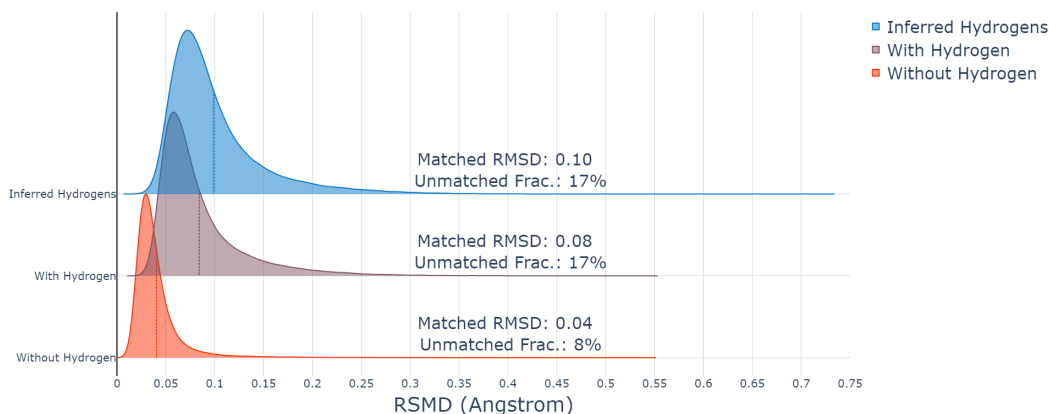


Figure 4: RMSD distribution for three autoencoder models on the full QM9 dataset. The models omit, reconstruct, and infer the locations of hydrogen atoms, respectively. Fraction of molecules which where all atoms could not be uniquely matched are noted for each model.

Some molecular datasets are published with absent, fuzzy, or incomplete hydrogen information. It is therefore useful to have embedding models appropriate for either the presence or absence of hydrogens. Thanks to the flexibility of our approach, we can easily test the model’s ability to accurately place hydrogen atoms given an input where hydrogen atoms have been removed.

4 Results

4.1 Autoencoder performance

We begin by assessing the reconstruction performance of the Mo3ENet autoencoder on the QM9 dataset under three conditions: (1) no hydrogens in input or output, and RMSD calculated on heavy atoms only, (2) hydrogens in input and output, with RMSD calculated on all atoms, and (3), no hydrogens in input, but hydrogen positions inferred in output, with RMSD calculated on all atoms.

Training results are summarized in Figure 4, where we show the distribution of RMSDs for the three cases, for the samples where input and input atoms could be uniquely matched by our scaffolding algorithm. All three models converge well with mean RMSDs $\leq 0.1\text{\AA}$, and with a reasonably tight distribution about the mean. We note for each model the mean deviation and fraction of the dataset for which the scaffolding failed to uniquely match inputs to outputs. These generally correspond to cases where either the output swarm was too diffuse to be neatly clustered, or where one or more atoms were simply not properly captured, even if the rest of the molecule is correct.

A significant positive correlate of error is the fraction of fluorine in each molecule, which should, perhaps, not be surprising since fluorine is by far the rarest atom type in the dataset. Possibly, even relatively coarse sample augmentation such as substituting hydrogens for fluorines in some samples could improve generalization in this dimension, though we avoided such tinkering in this study. All models overfit the reconstruction loss to some degree, and so it seems likely that improved performance could be achieved on larger datasets, or with additional hyperparameter tuning.

In Figure 5, we map the latent space of the autoencoder embedding in a reduced dimensional space. There is an open choice of which form of the embedding to visualize here, the full vector embedding, the scalarized embedding which includes a learned angular projection, or simply the Cartesian norms of the vector embedding. We chose the scalarized output (details of ‘scalarizer’ in SM), since it should contain richer information than the raw vector norms, including primarily the relative directions of vector components, and is invariant to molecule pose, which could over-complicate the mapping.

We employ UMAP [57], a dimensionality reduction algorithm, similar in spirit to principal component analysis [58], or t-distributed stochastic neighborhood embedding [59], which attempts to preserve relative distances between samples, such that samples which are near or far in the high dimensional

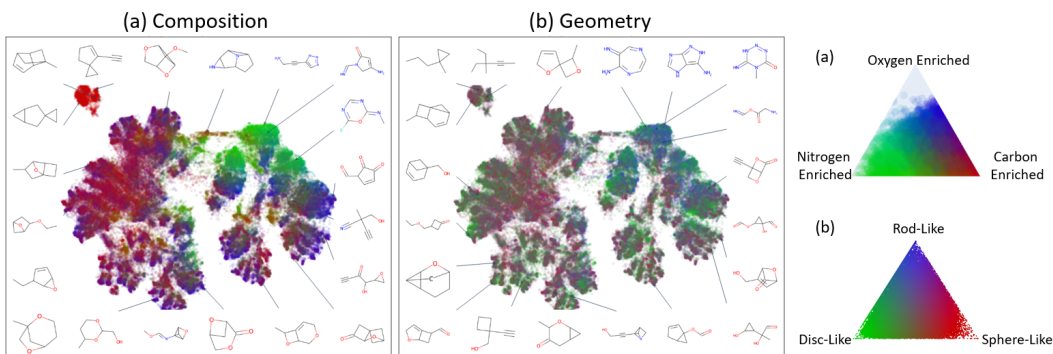


Figure 5: The UMAP decomposition for the full QM9 dataset according to our autoencoder trained with hydrogens, with the x and y axes the UMAP reduced dimensions of the 512 dimensional encoder embedding. Points are color coded according to compositional (atom fraction) and geometric molecular (principal inertial ratios) factors, with legends for each on the right hand side.

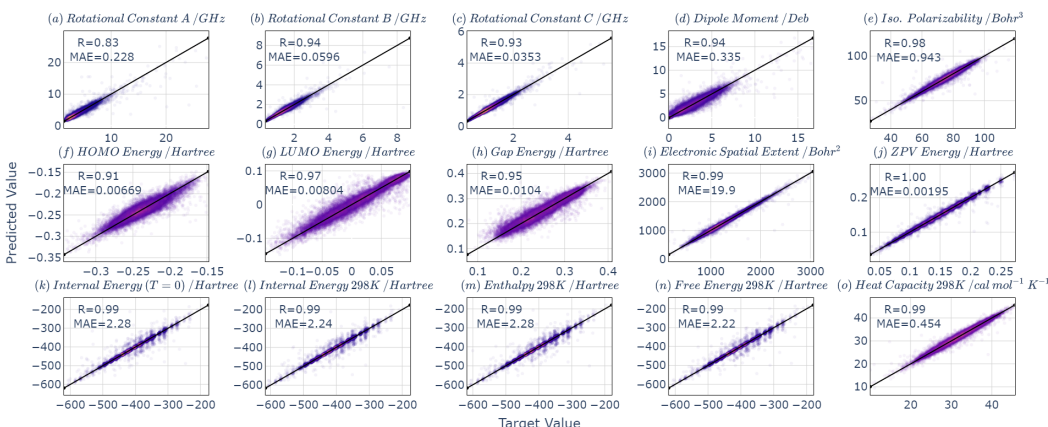


Figure 6: Predicted vs. true values on the test dataset (20% of sample) for the 15 QM9 quantum mechanical scalar properties, with associated correlation coefficients and mean absolute errors.

latent space are similarly placed in the reduced dimension. For visualization purposes, we generated 2-component projections from the scalarized embedding vectors of the full QM9 dataset, shown in Figure 5(a)-(b) together with various molecules noted in the margins, and colors assigned according to (a) relative atomic compositions and (b) shapes.

In Figure 5(a) we see quite distinctive clustering following relative elemental enrichment, particularly of nitrogenous compounds. In Figure 5(b), we see that the relative molecular geometries, as expressed by principal moments of inertia are also differentiated, indicating separation according to molecular shapes. Overall, this analysis shows that the model is learning a chemically meaningful embedding, which incorporates information on molecular composition and structure, as opposed to simply memorizing unconnected molecules in a large latent space.

4.2 Property prediction

With a trained encoder in hand, we proceed to scalar molecular property prediction. We freeze the encoder weights and train separate EMLP models for regression of the 15 QM9 properties, directly on the molecule embeddings, omitting the decoder. Regression hyperparameters and training details are given in the SM. We found that the overall performance was relatively insensitive to the details of the regression head, and use the same architecture for all properties.

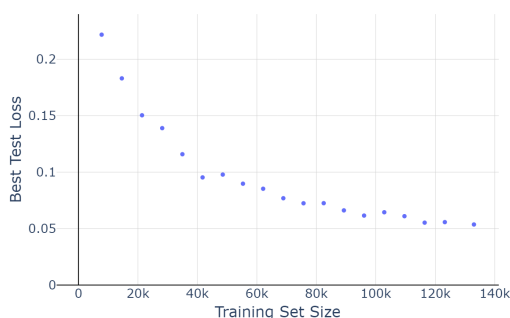


Figure 7: Training curve for regression of the HOMO-LUMO gap, showing the test loss minimum for each training run, as a function of total dataset size.

In Figure 6, the regression results on the 15 molecular properties of the QM9 database are presented. Although our results do not surpass prior works with exhaustively pretrained encodings [18], errors are small across the board, indicating that the learned embedding is both complete in the sense of containing all the relevant molecular information, and well enough regularized that models trained on top of it are able to generalize well to the test data.

A caveat to this is, as we see in Figure 7, dataset size is clearly limiting generalization performance, and we observed significant overfitting in training. This is likely due to both the architecture of the regression head and complexity of the embedding.

5 Discussion

We introduce and evaluate a new autoencoder architecture and reconstruction loss for the unsupervised learning of multi-type point clouds. This tool ‘solves’ the molecule representation problem in the limit of large data, in the sense that it can encode type, conformation, and pose information of a molecule in a provably complete embedding, via a sufficiently large and well trained autoencoder model. The main practical limitations of such a model are governed by the ability to efficiently optimize its parameters as well as the size and composition of the training dataset (equilibrium vs. non-equilibrium structures, molecule composition and size, etc.). The embedding quality on any new samples can, however, be trivially evaluated by decoding the sample and computing the reconstruction loss.

Beyond high-fidelity reconstructions, we further proved the quality of the molecule embedding as an input for regressing the fifteen QM9 molecular properties. The good performance on test data indicates that the embedding is to a certain extent physically meaningful, in contrast to a model that simply memorizes the dataset in a very large latent dimension. This point is buttressed by our embedding analyses, where we show visually that the model is clustering functional groups and structural motifs in its embedding space.

This work opens the door to several interesting applications. First, via training on larger and more diverse datasets, we can develop a universal/foundational representation model for high-fidelity encoding of molecule and pose information with this approach. Such a tool could be useful for molecule property prediction, similarity analysis/clustering, and conditioning for downstream learning tasks. The speed and generality of our approach also make it attractive as a generative model. The freedom of the decoder to generate structures with arbitrary numbers, types, and positions of atoms, and the latent space’s amenability to conditioning, is tantalizing to explore further. Finally, such a pretrained molecule embedding will be very useful in future exploration of molecule clusters and materials.

Acknowledgements

The authors would like to thank Mihail Bogojeski for valuable discussions. JR acknowledges financial support from the Deutsche Forschungsgemeinschaft (DFG) through the Heisenberg Programme

project 428315600. MK, JR, and MET acknowledge funding from grants from the National Science Foundation, DMR-2118890, and MET from CHE-1955381. This work was supported in part through the NYU IT High Performance Computing resources, services, and staff expertise.

References

- [1] Ben Fei, Weidong Yang, Wen-Ming Chen, Zhijun Li, Yikang Li, Tao Ma, Xing Hu, and Lipeng Ma. Comprehensive review of deep learning-based 3d point cloud completion processing and analysis. *IEEE Transactions on Intelligent Transportation Systems*, 23(12):22862–22883, 2022.
- [2] Yaoqing Yang, Chen Feng, Yiru Shen, and Dong Tian. Foldingnet: Point cloud auto-encoder via deep grid deformation. In *Proceedings of the IEEE conference on computer vision and pattern recognition*, pages 206–215, 2018.
- [3] Sergey N. Pozdnyakov and Michele Ceriotti. Incompleteness of graph neural networks for points clouds in three dimensions. *Machine Learning: Science and Technology*, 3(4):1–7, 2022.
- [4] Tuan Le, Frank Noe, and Djork-Arné Clevert. Representation learning on biomolecular structures using equivariant graph attention. In *Learning on Graphs Conference*, pages 1–17, 2022.
- [5] Shengchao Liu, Hongyu Guo, and Jian Tang. Molecular geometry pretraining with se (3)-invariant denoising distance matching. In *International Conference on Learning Representations*, 2022.
- [6] Ivan Žugec, R Matthias Geilhufe, and Ivor Lončarić. Global machine learning potentials for molecular crystals. *The Journal of chemical physics*, 160(15), 2024.
- [7] Michael Kilgour, Jutta Rogal, and Mark Tuckerman. Geometric deep learning for molecular crystal structure prediction. *Journal of chemical theory and computation*, 19(14):4743–4756, 2023.
- [8] John E Carpenter and Michael Grunwald. Pre-nucleation clusters predict crystal structures in models of chiral molecules. *Journal of the American Chemical Society*, 143(51):21580–21593, 2021.
- [9] Olga Egorova, Roohollah Hafizi, David C. Woods, and Graeme M. Day. Multifidelity Statistical Machine Learning for Molecular Crystal Structure Prediction. *Journal of Physical Chemistry A*, 124(39):8065–8078, 2020.
- [10] Rose K. Cersonsky, Maria Pakhnova, Edgar A. Engel, and Michele Ceriotti. A data-driven interpretation of the stability of organic molecular crystals. *Chemical Science*, 14(5):1272–1285, 2023.
- [11] Rithwik Tom, Timothy Rose, Imanuel Bier, Harriet O’Brien, Álvaro Vázquez-Mayagoitia, and Noa Marom. Genarris 2.0: A random structure generator for molecular crystals. *Computer Physics Communications*, 250:107170, 2020.
- [12] Ryan S. Defever, Colin Targonski, Steven W. Hall, Melissa C. Smith, and Sapna Sarupria. A generalized deep learning approach for local structure identification in molecular simulations. *Chemical Science*, 10(32):7503–7515, 2019.
- [13] Amit Kadan, Kevin Ryczko, Andrew Wildman, Rodrigo Wang, Adrian Roitberg, and Takeshi Yamazaki. Accelerated organic crystal structure prediction with genetic algorithms and machine learning. *Journal of Chemical Theory and Computation*, 19(24):9388–9402, 2023.
- [14] Jonas Köhler, Michele Invernizzi, Pim de Haan, and Frank Noé. Rigid Body Flows for Sampling Molecular Crystal Structures. *Proceedings of Machine Learning Research*, 202:17301–17326, 2023.
- [15] Joannis Apostolakis, Detlef Walter Maria Hofmann, and Thomas Lengauer. Derivation of a scoring function for crystal structure prediction. *Acta Crystallographica Section A: Foundations of Crystallography*, 57(4):442–450, 2001.

- [16] Zhichun Guo, Kehan Guo, Bozhao Nan, Yijun Tian, Roshni G Iyer, Yihong Ma, Olaf Wiest, Xiangliang Zhang, Wei Wang, Chuxu Zhang, et al. Graph-based molecular representation learning. *arXiv preprint arXiv:2207.04869*, 2022.
- [17] Oliver Wieder, Stefan Kohlbacher, Méline Kuenemann, Arthur Garon, Pierre Ducrot, Thomas Seidel, and Thierry Langer. A compact review of molecular property prediction with graph neural networks. *Drug Discovery Today: Technologies*, 37:1–12, 2020.
- [18] Gengmo Zhou, Zhifeng Gao, Qiankun Ding, Hang Zheng, Hongteng Xu, Zhewei Wei, Linfeng Zhang, and Guolin Ke. Uni-mol: A universal 3d molecular representation learning framework. In *International Conference on Learning Representations*, 2022.
- [19] Bowen Jing, Gabriele Corso, Jeffrey Chang, Regina Barzilay, and Tommi Jaakkola. Torsional Diffusion for Molecular Conformer Generation. *Advances in Neural Information Processing Systems*, 35:1–5, 2022.
- [20] Minkai Xu, Lantao Yu, Yang Song, Chence Shi, Stefano Ermon, and Jian Tang. Geodiff: A geometric diffusion model for molecular conformation generation. In *International Conference on Learning Representations*, 2021.
- [21] Minkai Xu, Alexander S Powers, Ron O Dror, Stefano Ermon, and Jure Leskovec. Geometric latent diffusion models for 3d molecule generation. In *International Conference on Machine Learning*, pages 38592–38610, 2023.
- [22] Emiel Hoogeboom, Victor Garcia Satorras, Clément Vignac, and Max Welling. Equivariant diffusion for molecule generation in 3d. In *International conference on machine learning*, pages 8867–8887, 2022.
- [23] Kristof Schütt, Oliver Unke, and Michael Gastegger. Equivariant message passing for the prediction of tensorial properties and molecular spectra. In *International Conference on Machine Learning*, pages 9377–9388, 2021.
- [24] Congyue Deng, Or Litany, Yueqi Duan, Adrien Poulénard, Andrea Tagliasacchi, and Leonidas J Guibas. Vector neurons: A general framework for so(3)-equivariant networks. In *Proceedings of the IEEE/CVF International Conference on Computer Vision*, pages 12200–12209, 2021.
- [25] Charles R Qi, Hao Su, Kaichun Mo, and Leonidas J Guibas. Pointnet: Deep learning on point sets for 3d classification and segmentation. In *Proceedings of the IEEE conference on computer vision and pattern recognition*, pages 652–660, 2017.
- [26] Lyne P Tchapmi, Vineet Kosaraju, Hamid Rezafofighi, Ian Reid, and Silvio Savarese. Topnet: Structural point cloud decoder. In *Proceedings of the IEEE/CVF conference on computer vision and pattern recognition*, pages 383–392, 2019.
- [27] Yulan Guo, Hanyun Wang, Qingyong Hu, Hao Liu, Li Liu, and Mohammed Bennamoun. Deep learning for 3d point clouds: A survey. *IEEE transactions on pattern analysis and machine intelligence*, 43(12):4338–4364, 2020.
- [28] Jiaying Zhang, Xiaoli Zhao, Zheng Chen, and Zhejun Lu. A review of deep learning-based semantic segmentation for point cloud. *IEEE access*, 7:179118–179133, 2019.
- [29] Pratik Suchde, Thibault Jacquemin, and Oleg Davydov. Point cloud generation for meshfree methods: An overview. *Archives of Computational Methods in Engineering*, 30(2):889–915, 2023.
- [30] Jiaxin Li, Yingcai Bi, and Gim Hee Lee. Discrete rotation equivariance for point cloud recognition. In *International conference on robotics and automation*, pages 7269–7275. IEEE, 2019.
- [31] Clément Vignac, Andreas Loukas, and Pascal Frossard. Building powerful and equivariant graph neural networks with structural neural message-passing. *Advances in neural information processing systems*, 33:14143–14155, 2020.

- [32] Nicolas Keriven and Gabriel Peyré. Universal invariant and equivariant graph neural networks. *Advances in Neural Information Processing Systems*, 32, 2019.
- [33] Victor Garcia Satorras, Emiel Hoogeboom, and Max Welling. E (n) equivariant graph neural networks. In *International conference on machine learning*, pages 9323–9332, 2021.
- [34] Jaesung Choe, ByeongIn Joung, Francois Rameau, Jaesik Park, and In So Kweon. Deep point cloud reconstruction. In *International Conference on Learning Representations*, 2021.
- [35] Maciej Zamorski, Maciej Zięba, Piotr Klukowski, Rafał Nowak, Karol Kurach, Wojciech Stokowiec, and Tomasz Trzciński. Adversarial autoencoders for compact representations of 3D point clouds. *Computer Vision and Image Understanding*, 193, 2020.
- [36] Li Jiang, Shaoshuai Shi, Xiaojuan Qi, and Jiaya Jia. Gal: Geometric adversarial loss for single-view 3d-object reconstruction. In *Proceedings of the European conference on computer vision*, pages 802–816, 2018.
- [37] Soroush Ahmadi, Mohammad Amin Ghanavati, and Sohrab Rohani. Machine learning-guided prediction of cocrystals using point cloud-based molecular representation. *Chemistry of Materials*, 2024.
- [38] Katja Hansen, Franziska Biegler, Raghunathan Ramakrishnan, Wiktor Pronobis, O Anatole Von Lilienfeld, Klaus-Robert Müller, and Alexandre Tkatchenko. Machine learning predictions of molecular properties: Accurate many-body potentials and nonlocality in chemical space. *The journal of physical chemistry letters*, 6(12):2326–2331, 2015.
- [39] Matthias Rupp, Alexandre Tkatchenko, Klaus-Robert Müller, and O Anatole Von Lilienfeld. Fast and accurate modeling of molecular atomization energies with machine learning. *Physical review letters*, 108(5):058301, 2012.
- [40] Albert P Bartók, Risi Kondor, and Gábor Csányi. On representing chemical environments. *Physical Review B*, 87(18):184115, 2013.
- [41] Felix Musil, Andrea Grisafi, Albert P. Bartók, Christoph Ortner, Gábor Csányi, and Michele Ceriotti. Physics-Inspired Structural Representations for Molecules and Materials. *Chem. Rev.*, 121(16):9759–9815, August 2021.
- [42] Kevin Yang, Kyle Swanson, Wengong Jin, Connor Coley, Philipp Eiden, Hua Gao, Angel Guzman-Perez, Timothy Hopper, Brian Kelley, Miriam Mathea, Andrew Palmer, Volker Settels, Tommi Jaakkola, Klavs Jensen, and Regina Barzilay. Analyzing Learned Molecular Representations for Property Prediction. *Journal of Chemical Information and Modeling*, 59(8):3370–3388, 2019.
- [43] Yuyang Wang, Jianren Wang, Zhonglin Cao, and Amir Barati Farimani. Molecular contrastive learning of representations via graph neural networks. *Nature Machine Intelligence*, 4(3): 279–287, 2022.
- [44] Shampa Raghunathan and U Deva Priyakumar. Molecular representations for machine learning applications in chemistry. *International Journal of Quantum Chemistry*, 122(7):e26870, 2022.
- [45] Jiaxuan You, Rex Ying, Xiang Ren, William Hamilton, and Jure Leskovec. Graphrnn: Generating realistic graphs with deep auto-regressive models. In *International conference on machine learning*, pages 5708–5717, 2018.
- [46] Robin Winter, Frank Noé, and Djork-Arné Clevert. Auto-encoding molecular conformations. *arXiv preprint arXiv:2101.01618*, 2021.
- [47] Sunghoon Joo, Min Soo Kim, Jaeho Yang, and Jaehyun Park. Generative Model for Proposing Drug Candidates Satisfying Anticancer Properties Using a Conditional Variational Autoencoder. *ACS Omega*, 5(30):18642–18650, 2020.
- [48] Martin Simonovsky and Nikos Komodakis. Graphvae: Towards generation of small graphs using variational autoencoders. In *International Conference on Artificial Neural Networks*, pages 412–422, 2018.

- [49] Mingyuan Xu, Weifeng Huang, Min Xu, Jinping Lei, and Hongming Chen. 3d conformational generative models for biological structures using graph information-embedded relative coordinates. *Molecules*, 28(1):321, 2022.
- [50] Agnieszka Ilnicka and Gisbert Schneider. Designing molecules with autoencoder networks. *Nature Computational Science*, 3(11):922–933, 2023.
- [51] Shriram Chennakesavalu, David J Toomer, and Grant M Rotskoff. Ensuring thermodynamic consistency with invertible coarse-graining. *The Journal of Chemical Physics*, 158(12), 2023.
- [52] Lars Ruddigkeit, Ruud Van Deursen, Lorenz C Blum, and Jean-Louis Reymond. Enumeration of 166 billion organic small molecules in the chemical universe database gdb-17. *Journal of chemical information and modeling*, 52(11):2864–2875, 2012.
- [53] Raghunathan Ramakrishnan, Pavlo O Dral, Matthias Rupp, and O Anatole Von Lilienfeld. Quantum chemistry structures and properties of 134 kilo molecules. *Scientific data*, 1(1):1–7, 2014.
- [54] Colin R Groom, Ian J Bruno, Matthew P Lightfoot, and Suzanna C Ward. The cambridge structural database. *Acta Crystallographica Section B: Structural Science, Crystal Engineering and Materials*, 72(2):171–179, 2016.
- [55] Simon Axelrod and Rafael Gomez-Bombarelli. Geom, energy-annotated molecular conformations for property prediction and molecular generation. *Scientific Data*, 9(1):185, 2022.
- [56] Clemens Isert, Kenneth Atz, José Jiménez-Luna, and Gisbert Schneider. Qmugs, quantum mechanical properties of drug-like molecules. *Scientific Data*, 9(1):273, 2022.
- [57] Leland McInnes, John Healy, and James Melville. Umap: Uniform manifold approximation and projection for dimension reduction. *arXiv preprint arXiv:1802.03426*, 2018.
- [58] Karl Pearson. Liii. on lines and planes of closest fit to systems of points in space. *The London, Edinburgh, and Dublin philosophical magazine and journal of science*, 2(11):559–572, 1901.
- [59] Geoffrey E Hinton and Sam Roweis. Stochastic neighbor embedding. In S. Becker, S. Thrun, and K. Obermayer, editors, *Advances in Neural Information Processing Systems*, volume 15 of *NIPS’02*, page 857–864. MIT Press, 2002.
- [60] Yunsheng Shi, Zhengjie Huang, Shikun Feng, Hui Zhong, Wenjing Wang, and Yu Sun. Masked Label Prediction: Unified Message Passing Model for Semi-Supervised Classification. In *IJCAI International Joint Conference on Artificial Intelligence*, pages 1548–1554, 2021. ISBN 9780999241196.
- [61] Ilya Loshchilov and Frank Hutter. Decoupled weight decay regularization. In *International Conference on Learning Representations*, 2018.

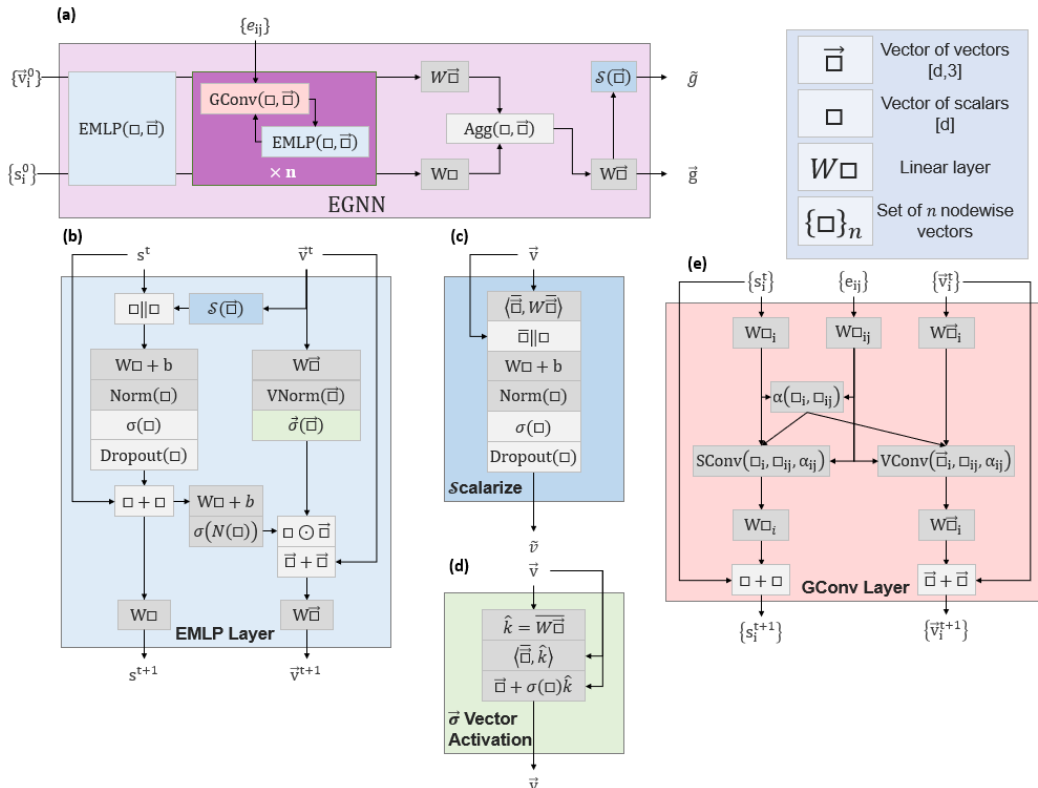


Figure A1: Panels (a), (b), (c), (d), and (e) outline the architecture for the graph neural net, equivariant multilayer perceptron, scalarizer, vector activation, and graph convolution modules, respectively. Dark grey nodes represent functions with learnable weights, and lighter grey functions without.

A Supplemental material

A.1 Details of Model Architecture

The EMLP layer acts on scalar inputs s of dimension $[n, k]$ and vector inputs \vec{v} of dimension $[n, 3, l]$. The scalar track is a standard neural network layer with linear transformation, normalization, activation, dropout, and residual connection, with optional dimension adjustment between layers,

$$s^{t+1} = \mathbf{W}_2^t (s^t + \text{D}(\sigma(\text{N}(\mathbf{W}_1^t(s^t \parallel \vec{v}^t) + \mathbf{b}^t))))), \quad (6)$$

and scalarized representation of the vector track $\tilde{v} = \mathcal{S}(\vec{v})$ concatenated before the linear operation. \tilde{v} is computed following panel (c) of Figure A1, and encodes pose-invariant information from \vec{v} , including the vector norms and relative internal angles. Following again the insight of [24], we learn a set of internal equivariant axes (in practice, three axes) within the normalized vector directions via $\mathbf{W}\tilde{v}$, with $\tilde{v} = \frac{\vec{v}}{\|\vec{v}\|}$ and compute their overlaps to \tilde{v} . This comprises a transform from the original Cartesian basis to a learned internal basis which rotates equivariantly with the molecule. We then concatenate this to the vector norms and pass them through a linear layer, treating them as regular invariant scalars. The obvious alternative to this ‘scalarization’ scheme is to simply take the euclidean norm of \vec{v} and use it as the ‘scalar representation’ of \vec{v} . While reasonable in principle, this leaves invariant information about the relative directions of vectors on the table, and so \tilde{v} should provide a richer scalar picture than \vec{v} .

The vector side of the forward pass is analogous to the scalar, but with adjustments to retain equivariance.

$$\begin{aligned} \mathbf{s}_g &= \sigma(\mathbf{N}(\mathbf{W}^t \mathbf{s}^{t+1} + \mathbf{b}_s^t)), \\ \vec{\mathbf{v}}_g &= \vec{\sigma}(\vec{\mathbf{N}}(\mathbf{W}^t \vec{\mathbf{v}}^t)), \\ \vec{\mathbf{v}}^{t+1} &= \mathbf{W}^t (\vec{\mathbf{v}}^t + \mathbf{s}_g \odot \vec{\mathbf{v}}_g). \end{aligned} \quad (7)$$

First, we pass information from the scalar track to act as a rescaling factor for vector norms. Then, we transform the vector features using modified vector normalization, $\vec{\mathbf{N}}$, operating only on vector norms, and vector activation $\vec{\sigma}$ (see Fig. A1 panel (d)), following the scheme in [24]. Finally, the residual is re-added and if required the dimension is adjusted for the next layer.

The graph model in the encoder follows alternating EMLP and graph convolution layers. Before node embedding, point positions are first normalized by a radial factor equal to the largest molecular radius in the full dataset. The initial node embedding sets scalar and vector features for each point in the input cloud,

$$\begin{aligned} \mathbf{x}_i^0 &= \mathbf{W} (\mathbf{E}_{z_i} |\bar{r}_i|) + \mathbf{b} \\ \vec{\mathbf{v}}_i^0 &= \mathbf{W} \vec{r}_i \end{aligned} \quad (8)$$

with \vec{r}_i the vector from the molecule centroid to atom i , \bar{r}_i the norm of \vec{r}_i , and \mathbf{E}_{z_i} a learned embedding of the atom type z_i .

Graph convolution again comprises a scalar and vector track, with the scalar track using the ‘TransformerConv’ module [60], an efficient and expressive graph convolution which combines neighboring nodes according to a coefficient α_{ij} learned via the self-attention mechanism,

$$\alpha_{ij} = \text{Softmax} \left(\frac{(\mathbf{W}_1 \mathbf{S}_i)^T (\mathbf{W}_2 \mathbf{S}_j + \mathbf{W}_3 \mathbf{E}_{ij})}{\sqrt{d}} \right), \quad (9)$$

with $\mathbf{S}_i = \mathbf{W} \mathbf{s}^t$ and $\mathbf{E}_{ij} = \mathbf{W} \mathbf{e}_{ij}$ as node and edge embeddings for message passing respectively. Scalar messages are passed according to

$$\mathbf{S}_i^{t+1} = \beta_i \mathbf{W}_1 \mathbf{S}_i^t + (1 - \beta_i) \sum_{j \in r_c} \alpha_{ij} (\mathbf{W}_2 \mathbf{S}_j^t + \mathbf{W}_3 \mathbf{E}_{ij}), \quad (10)$$

with $j \in r_c$ the nodes j within the cutoff range r_c of node i . Vector messages are passed according to an equivariant attention function with shared attention weights from the scalar message passing, where we gate against the edge contributions rather than adding to maintain equivariance,

$$\vec{\mathbf{V}}_i^{t+1} = \mathbf{W}_1 \vec{\mathbf{V}}_i^t + \sum_{j \in r_c} \alpha_{ij} (\mathbf{W}_2 \vec{\mathbf{V}}_j^t \cdot \mathbf{W}_3 \mathbf{E}_{ij}). \quad (11)$$

After graph convolution, we aggregate nodewise information via a softmax weighting over the channel dimension,

$$\vec{\mathbf{g}}_k = \sum_i^{n_i} \left(\frac{e^{\vec{\mathbf{v}}_{ik}}}{\sum_j^{n_i} e^{\vec{\mathbf{v}}_{jk}}} \right) \vec{\mathbf{v}}_{ik}. \quad (12)$$

All codes and training scripts are available at our archived GitHub repository here.

A.2 Model hyperparameters and optimization

A single training run of one of our autoencoder models on QM9 took 1-2 days on an NVIDIA V100 GPU. A QM9 property regression run took 1-3 hours on the same hardware. Over the course of the project, several hundred partial and complete runs were undertaken for the development of the new architecture and loss model, and to identify hyperparameter regimes with fast convergence to high quality loss minima. We found by experimentation that different hyperparameters significantly impacted the generalization and training speed of the autoencoder model. Here, we give the best parameters found to-date, which were used for the results shown in the main text.

Encoder: GeLU activation, atom type embedding dimension of 32, graph convolution cutoff of 14\AA , 5% dropout probability in nodewise fully-connected layers, node embedding dimension, graph readout dimension and bottleneck dimension all 512, 4 fully-connected layers per EMLP block, message dimension of 128, 16 attention heads, graph-wise layer normalization, 1 convolutional layer, and 32 Gaussian radial basis functions.

Decoder: GeLU activation, 5% dropout probability, hidden dimension of 512, 512 nodes in the output swarm, and 1 fully-connected layer.

Autoencoder Optimization: AdamW [61] optimizer with weight decay of 0.05, initial learning rate of $5.0\text{E-}5$, ramping to $1.0\text{E-}3$, then down to $1.0\text{E-}6$. Batch size starting at 50 and ramping to 2522 (maxes out our GPU memory). The Gaussian width is initialized at 1.05, and reduced by 1% when the reconstruction test loss reaches 0.01, until the mean sample self-overlap reaches $5.0\text{E-}4$.

Embedding Regressor: GeLU activation, 10% dropout probability, hidden dimension of 128, and 4 fully-connected layers.

Regressor Optimization: AdamW optimizer with weight decay of 0.1, initial learning rate of $1.0\text{E-}4$, ramping to $5.0\text{E-}4$, then down to $5.0\text{E-}6$. Batch size starting at 50 and ramping to 2000.